Thermal stability of M_xO_y doped zirconia aerogels (M = Y, Yb, Gd, Ce, Ca) studied through 1200°C

Nathaniel S. Olson[1], Frances I. Hurwitz[2], Jamesa L. Stokes[2], Haiquan Guo[3], Richard B. Rogers[2], Jessica A. Krogstad[1,*]

[1]Department of Materials Science and Engineering, University of Illinois at Urbana-Champaign, Urbana, IL
[2]NASA Glenn Research Center, Cleveland, OH
[3]Universities Space Research Association, Cleveland, OH

Abstract

The high porosities and low densities of ceramic aerogels offer outstanding insulative performance in applications where weight is a critical factor. The high surface area-to-volume ratios and specific surface areas provide extremely low thermal conductivity, but also contribute to rapid densification of the pore structure at elevated temperatures. This densification diminishes their favorable properties and inhibits use of aerogels in high temperature applications. This work contributes to a design framework for thermally stable aerogels via the study of dopant chemistry (Y, Yb, Gd, Ca, Ce) in zirconia aerogels. The structural evolution was studied to 1200°C using nitrogen physisorption, scanning electron microscopy, and x-ray diffraction. The role of dopant identity and concentration in thermal stability was elucidated. In context of the design framework, dopant chemistry is an aggregate for many closely related material properties, each of which may contribute to aerogel structural evolution. To develop a truly predictive design framework for ceramic-based aerogels, systematic and comprehensive evaluation of thermodynamic and kinetic properties must be performed in conjunction with studies on structural evolution.

Keywords: aerogel, zirconia, thermal management, porous ceramics

* Corresponding author (jakrogst@illinois.edu)

Introduction

The extreme environments experienced in aerospace applications necessitate advanced thermal management materials that can protect critical underlying structures. The development of highly insulating and lightweight thermal management materials remains a significant challenge. Materials with lower thermal conductivity allow for higher operating temperatures in more extreme environments. Materials with low density reduce the overall mass of thermal management systems, reducing cost and improving payload capacity. A promising class of highly porous materials are aerogels. Exceeding 90% porosity, aerogels are extremely lightweight and have extraordinarily low thermal conductivities.[1] The highly porous structure of aerogels contributes to favorable properties for use as lightweight insulation but presents a critical challenge: thermal stability of the pore structure. The extremely high specific surface area (SSA) of aerogels result in large driving forces for sintering and densification upon heating, increasing the density and thermal conductivity. The integrity of the highly porous aerogel structure must be maintained to temperatures beyond 1200°C to enable use as insulation in the extreme environments of aerospace applications. The temperature and exposure time over which the material maintains high porosity and low thermal conductivity needs to be defined for various aerogel systems.

The term "aerogel" refers to a broad category of highly porous materials, spanning a wide range of compositions including polymers, metals, and metal oxides, borides, and chalcogenides. Polymer aerogels have favorable mechanical properties, but decompose at moderate temperatures, limiting their use below 500°C.[2, 3] Exploration of metal oxides, borides, and chalcogenides opens a vast area of compositional space for exploration leading to a wide range of reported thermal stabilities.[4] Silica aerogels are arguably the most studied type of aerogel, but sinter and densify rapidly beyond 700°C.[5–7] Alumina aerogels densify upon formation of α-alumina beyond 1000°C, but this can be improved upon by doping with yttria.[8] A significant leap in thermal stability was realized by introduction of silica to alumina aerogels and the use of a colloidal

boehmite precursor.[9] A variety of lanthanide oxides were found to lose most of their SSA after heating to 650°C.[10] Zirconia aerogels experienced a reduction in SSA from 282 m^2/g as dried to 92 m^2/g after two hours at 500°C.[11] However, a study on doping zirconia aerogels with yttria and ytterbia up to 15 mol% $MO_{1.5}$ improved the thermal stability and later work demonstrated yttria doping beyond 30 mol% $YO_{1.5}$ proved to be an even more effective means of improving the thermal stability of the pore structure.[12, 13] The latter work hypothesized that a reduction in surface energy (driving force for densification) and cation diffusivity (rate of densification) with higher yttria content contributed to the improvement in thermal stability.

To further evaluate the effect of composition and material properties on zirconia aerogel thermal stability, the study of other dopants, including ytterbium, gadolinium, cerium, and calcium, is warranted. Work in doped zirconias in the field of thermal barrier coatings (TBCs) have demonstrated the influence of dopants on the structure, properties, and structural evolution of the material. For TBCs, materials are sought with low thermal conductivity, high phase stability, high erosion resistance, and ease of processability. Modifying the dopant identity and concentration has been linked to changes in thermal conductivity and is established as a means of enabling advanced TBC material design.[14–19] A variety of rare earth dopant systems have been studied in the context of nanocrystalline zirconias, again with dopant identity and concentration changing the sintering and coarsening behavior of the materials.[20–25] Obtaining an understanding of how relevant kinetic and thermodynamic material properties, including surface energy, cation diffusivity, surface and grain boundary diffusivity, thermal conductivity and more, in doped zirconia influence thermal stability will contribute to the development and understanding a design framework to enable the intentional exploration of thermally stable aerogels. Previous work did this for YSZ aerogels: lower cation diffusivity and lower surface energy were identified as potential markers for improved thermal stability.[13, 26, 27] To further evaluate these hypotheses, study of a wider range of dopants and concentrations is necessary.

3

In this work, zirconia aerogels doped with 15 or 30 mol% M/(M+Zr) where M = Y, Yb, Gd, Ce, Ca are prepared to study the evolution of the aerogel structure as a function of composition to temperatures of 1200°C. The evolution of the microstructure, porosity, and crystal structure are characterized to assess thermal stability. Materials with improved thermal stability are expected to exhibit higher SSAs, constant pore size distributions, minimal crystallite growth, and maintenance of a single crystal phase. This study demonstrates again the impact of dopants on improving the thermal stability of zirconia aerogels but suggests limitations on the magnitude of thermal stability improvement achievable by tuning composition.

Methods/Procedure

Synthesis: Doped zirconia aerogels were prepared using a sol-gel synthesis adapted from previous work.[28] Metal salts utilized in this work were zirconyl chloride octahydrate ($ZrOCl_2 \cdot 8H_2O$, Alfa Aesar 99.9%), yttrium(III) chloride hexahydrate ($YCl_3 \cdot 6H_2O$, Acros Organics 99.9%), ytterbium(III) chloride hexahydrate ($YbCl_3 \cdot 6H_2O$, Sigma Aldrich 99.9%), gadolinium(III) chloride hexahydrate ($GdCl_3 \cdot 6H_2O$, Sigma Aldrich 99.9%), cerium(III) chloride heptahydrate ($CeCl_3 \cdot 7H_2O$, Sigma Aldrich 99.9%), and calcium(II) nitrate tetrahydrate ($Ca(NO_3)_2 \cdot 4H_2O$, Sigma-Aldrich 99.9%). Zirconyl chloride octahydrate and the dopant metal salt were dissolved in 200 proof ethanol (Decon Labs) in separate jars at a ratio of 1.263 mmol metal per mL ethanol. After 30 minutes of stirring, DI water was added at six times the stoichiometric amount needed to fully hydrolyze the metal salt. As an example, for each mole of Zr^{4+}, 24 moles of water were added. The precursor solutions were hydrolyzed under stirring for 60 minutes and were then combined and stirred for 15 minutes. The combined solution was placed in an ice bath to slow down the gelation reaction and propylene oxide (PO) (CH_3CHCH_2O, Sigma Aldrich) was added dropwise at a ratio of 2.342 mol PO per mole of metal. The solution was stirred for 5 minutes and transferred to molds made from polyethylene syringes (24 mL) with the top cut off. For consistency, the plunger was placed at 20 mL and the mold filled to the 10 mL mark. Gelation was generally

complete within 30 min. Parafilm was used to seal the mold and gels were held in the mold for 24 hours. Gels were then extracted into 200 proof ethanol and aged for 5 to 7 days. The aged gels were then supercritically dried using carbon dioxide, featuring four washes in liquid carbon dioxide before bringing the carbon dioxide to its supercritical state and evacuating the fluid.

Heat Treatments: Aerogels were heat treated in high purity alumina crucibles. Heat treatments were performed in a box furnace under air with a temperature ramp of 10°C/min to 600, 1000, or 1200°C, each with a 20-minute hold at the maximum temperature. Aerogels were cooled to room temperature within the furnace.

Characterization: The diameter and length of supercritically dried (as dried) aerogel monoliths were measured to characterize bulk density and shrinkage relative to the mold. Nitrogen physisorption measurements were performed using a Micromeritics 3Flex to measure specific surface area via the method of Brunauer-Emmett-Teller (BET) and pore volume and size via the method of Barret-Joyner-Halenda (BJH). Prior to physisorption analysis, samples were degassed under vacuum at 80°C with a heating rate of 5°C/min and a hold of 8 hours. Scanning electron microscopy (SEM) was conducted on a Hitachi S4800 SEM to characterize pore morphology and microstructure. Samples were crushed onto carbon tape and imaged uncoated at 2 kV, 10 μA, and a working distance of 5 mm. Powder x-ray diffraction (XRD) was used to identify the crystalline phase and calculate the crystallite size via the Scherrer equation. To prepare samples for XRD, powders were crushed in a mortar and pestle with a small amount of 200 proof ethanol. The suspension was dropped via pipette onto low background holders. XRD was performed on a Bruker D8 Advance (Cu Kα, 1.5406 Å) from 10 to 100° 2θ, 0.02 degrees per step, and 0.25 seconds per step. Parallel beam geometry was used with a 0.2 mm divergence slit and a panoramic Soller slit. Rietveld refinements and peak fitting were performed in GSAS II (v. 4783) to identify crystalline phase and calculate crystallite size.[29] Peak positions and widths were

exported and the Scherrer equation was applied to each. The reported crystallite size was obtained by taking the average of all peaks.

Statistics: Statistical tests were conducted in OriginPro 2021b (v. 9.8.5.212). For all statistical tests, a significance level (α) was selected of 0.05. Two-way ANOVAs were first applied with dopant and concentration as the two factors. For significant factor-response pairs, Tukey tests were employed to determine which levels of the factor had a significant effect on the response.

Results

1. Materials Synthesized

Zirconia (ZrO_2) aerogels were prepared at 15 and 30 mol% MO_x for M = Y, Yb, Gd, Ca, and Ce. The properties of these dopants are summarized in Table 1. Dopants were selected to vary charge, radius, and mass to explore the relationship between composition and thermal stability. From here, samples will be referred to as 15M or 30M (*e.g.*, 15Y, 30Y, 15Yb, etc.). Aerogels of all compositions successfully gelled and remained monolithic following supercritical drying. Qualitatively, the Y, Yb, and Gd were white and more opaque with increased dopant concentration. Ca-doped aerogels were also opaque but were markedly glassier and more brittle. Ce-doped aerogels appeared yellow with some signs of white streaking through the material.

Table 1: Precursor and cation properties for metal oxides under study. Cation radii are listed for a coordination number of 8. The cation charges below are assumptions. For Ce, the charge was assumed to be +3 for the precursor, but +4 following aerogel heat treatment.[30, 31]

M	Precursor	Cation Charge	Cation Radius (Å)	Cation Mass (amu)
Zr	$ZrOCl_2 \cdot 8H_2O$	+4	0.840	91.22
Y	$YCl_3 \cdot 6H_2O$	+3	1.019	88.91
Yb	$YbCl_3 \cdot 6H_2O$	+3	0.985	173.0
Gd	$GdCl_3 \cdot 6H_2O$	+3	1.053	157.2
Ca	$Ca(NO_3)_2 \cdot 4H_2O$	+2	1.120	40.08
Ce	$CeCl_3 \cdot 7H_2O$	+3/+4	0.970	140.01

2. As Dried Aerogels

The mass, diameter, and length of the aerogel monoliths were measured and averaged to obtain percent shrinkage and bulk density measurements. Nitrogen physisorption isotherms were used to calculate BET specific surface areas (SSA), BJH desorption cumulative pore volume (V_{BJH}), and BJH desorption average pore diameter (D_{BJH}). The summary of these results is tabulated in Table 2, with SSAs between 400 and 550 m^2/g and D_{BJH} from 14 to 27 nm. Increased dopant level was correlated with statistically significantly reduced shrinkage, with an average of 21.9% for 15 mol% and 15.2% for 30 mol% (p=0.012). The dopant identity did not have a bearing on shrinkage or density. The dopant level modified all aspects of the pore structure with increased dopant concentration leading to lower SSA (p=0.046), higher V_{BJH} (p=0.016), and higher D_{BJH} (p=0.022). The dopant identity only influenced SSA (p=0.042). A Tukey test indicated Gd (average SSA of 500 m^2/g) and Ce (average SSA of 428 m^2/g) were significantly different, with the other dopants lying between these extremes with no statistically significant difference.

Table 2: Measurements of porosity and physical structure for the as dried aerogels. In general, increased dopant results in lower shrinkage and coarser pore structures with lower SSA, larger D_{BJH}, and larger V_{BJH}.

M	mol % MO_x	SSA (m^2/g)	V_{BJH} (cm^3/g)	D_{BJH} (nm)	S (%)	ρ_b (g/cm^3)
Y	15	501	2.07	16.4	21.1	0.250

		SSA	V_{BJH}	D_{BJH}	S	ρ_b
	30	473	2.91	26.9	12.5	0.186
Yb	15	463	1.98	17.8	20.0	0.234
	30	452	2.29	19.1	12.9	0.220
Gd	15	532	2.10	14.5	19.6	0.230
	30	469	2.26	17.9	12.4	0.219
Ca	15	478	1.61	14.3	24.7	0.232
	30	463	2.43	22.6	23.8	0.208
Ce	15	437	1.73	16.7	24.0	0.281
	30	419	2.56	26.7	14.3	0.202

SSA = BET specific surface area
V_{BJH} = BJH desorption cumulative pore volume
D_{BJH} = BJH desorption average pore diameter
S = as dried shrinkage (diameter)
ρ_b = bulk density

Evaluation of BJH pore size distributions (PSD) in Figure 1 provided additional insight to the pore structures of the doped zirconia aerogels. Increased dopant level increased the average pore size and the PSD breadth for all dopants. The PSDs appeared remarkably similar at the same dopant level, regardless of dopant identity. 30 mol% MO_x consistently formed more disperse pore structures with a larger average pore size. Scanning electron microscopy (SEM) provided a qualitative look at the as dried pore structure as a function of dopant identity and level in Figure 2. In general, the pores appeared larger with more dispersity in size at higher dopant level, consistent with the BJH desorption pore sizes and distributions.
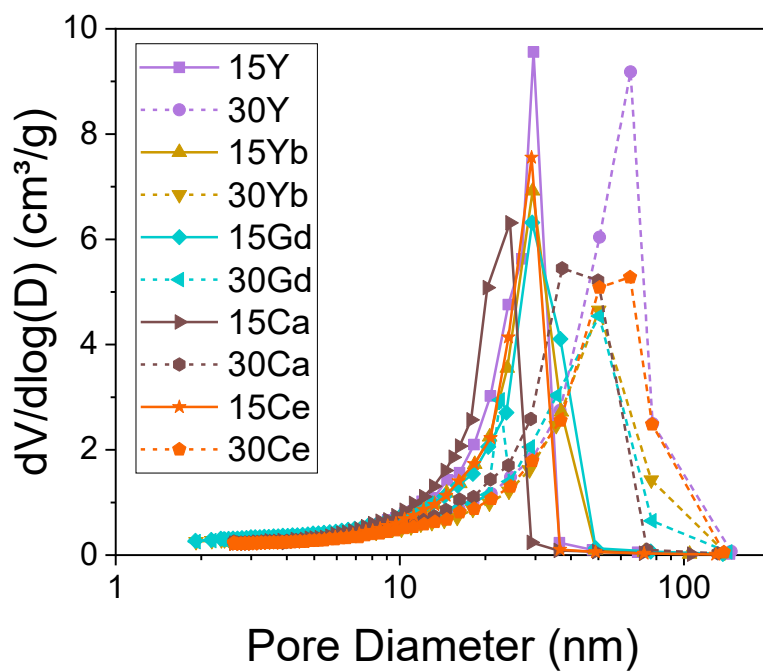
Figure 1: BJH desorption pore size distributions for as dried aerogels. For the as dried material, the distributions are grouped by dopant concentration with 15 mol% having a narrower distribution with smaller average pore size. Increased dopant concentration forms a broader distribution of larger pores.
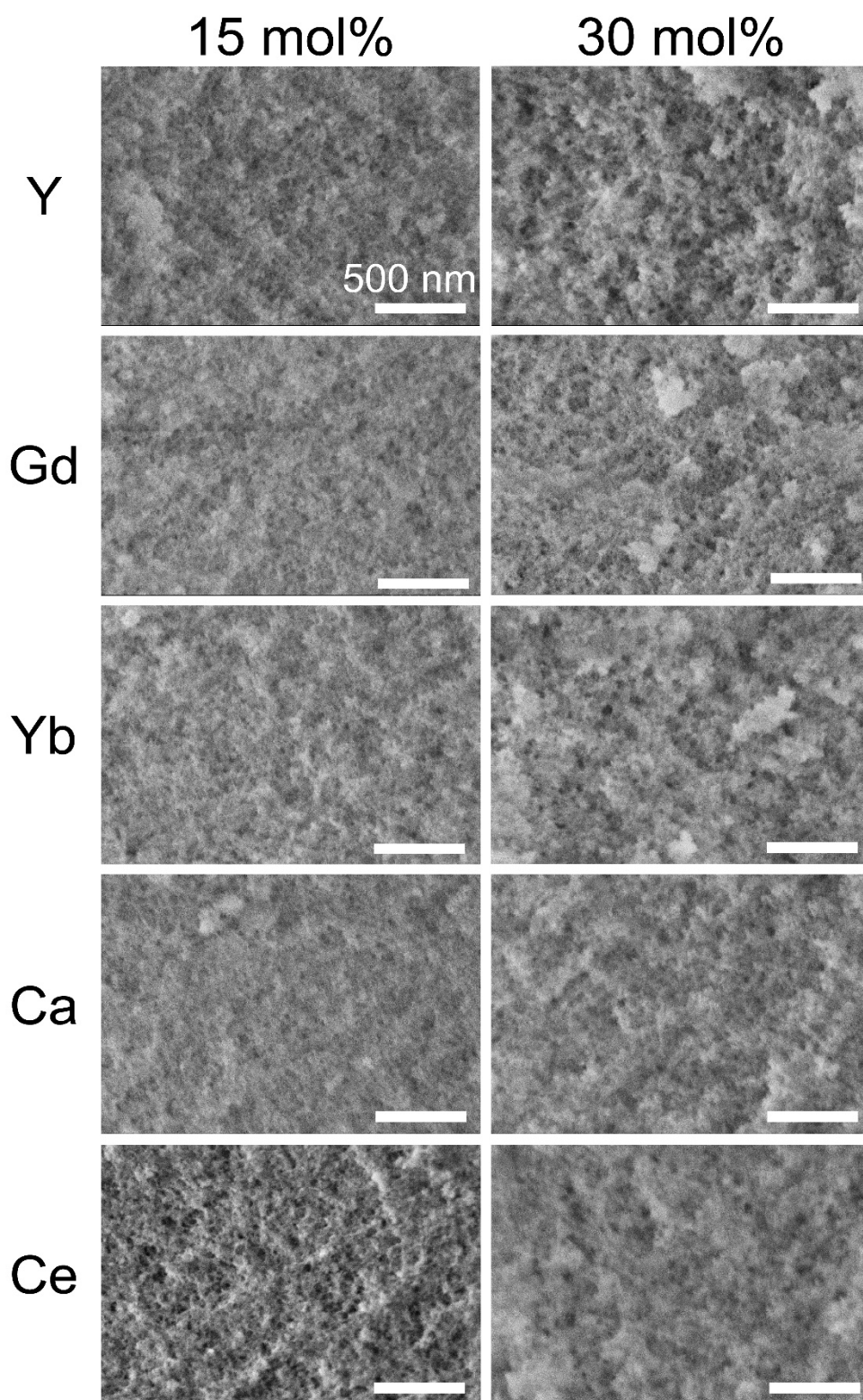
Figure 2: SEM images for the as dried aerogel samples. The scale bar is 500 nm in all images. In general, increased dopant concentration is associated with a more heterogenous population of pore sizes with larger pore size on average. SEM is capturing the macroporosity and does not have the resolution required to image mesoporosity directly.

2. Pore structure evolution with heat treatment

Nitrogen physisorption was performed on materials subjected to heat treatments of 600, 1000, and 1200°C. Following heat treatment, all samples underwent significant shrinkage and cracking that prevented the measurement of physical shrinkage. All samples maintained an opaque appearance with heat treatment. Thermal stability is defined as maximum SSA, maximum V_{BJH}, and minimum change in D_{BJH} following heat treatment. Figure 3(a-c) displays the change in SSA, V_{BJH}, and D_{BJH} for each composition as a function of temperature. The numerical values for each temperature can be found in Table S1 in the Supplementary Information. At 600°C, 30Y and 30Gd performed the best, maintaining SSAs of 166 and 140 m^2/g, respectively. At 1000°C, 30Y and 30Gd again maintained the highest SSAs of 47 and 50 m^2/g, respectively, with 30Ce also exhibiting notable stability with 49 m^2/g. Both Ce-doped samples were remarkably stable from 600 to 1200°C, as visible in the reduced slope of the SSA between these two temperatures. All samples underwent significant densification and loss of porosity by 1200°C with SSA generally reduced by an order of magnitude compared to 1000°C and two orders of magnitude compared to the as dried structure. Yet again, 30Y (16 m^2/g) and 30Gd (15 m^2/g) maintained over double the average SSA of all materials at 1200°C (7 m^2/g). Similar trends were observed in pore volume, with 30Y and 30Gd exhibiting the greatest pore volume at each temperature. In the Discussion, the evolution of these structures will be evaluated in a relative sense.

Figure 3(a-c): The evolution of (a) SSA, (b) V_{BJH}, and (c) D_{BJH} from as dried to 1200°C. As seen in the inset images in (a) and (b), increased dopant concentration has improved thermal stability, retaining higher SSA and V_{BJH} at 1000 and 1200°C. 30Y and 30Gd perform the best of all samples.
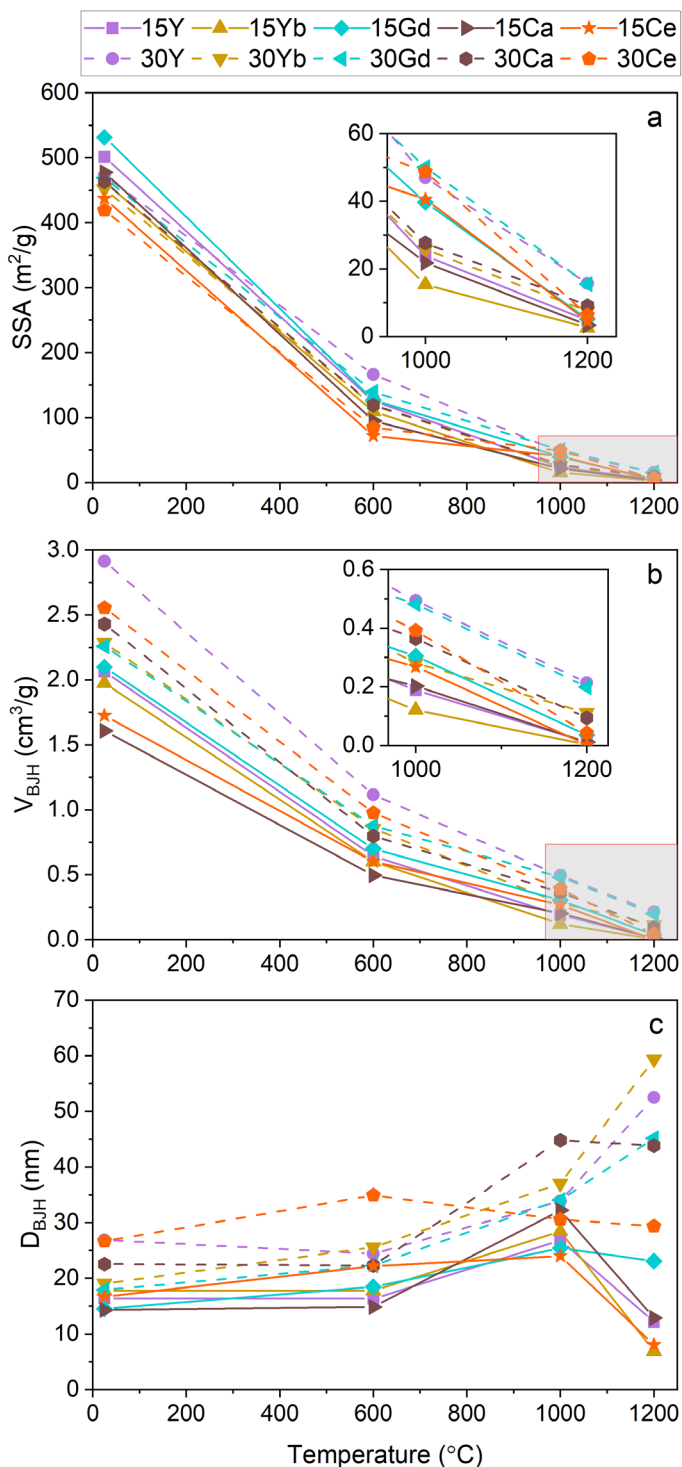
The evolution of pore size has no distinct trends to 1000°C, but from 1000 to 1200°C, all 30 mol% trivalent dopants (Y, Yb, Gd) grow in size while the same dopants at 15 mol% shrink in size.

Sufficient mass and sample area were utilized to minimize instrument error. Error bars are expected to be on the order of the marker size.

From statistical analysis, dopant level consistently had a significant effect on SSA, V_{BJH}, and D_{BJH} at all temperatures, with p-values for (SSA | V_{BJH} | D_{BJH}) of (600°C: p=0.027, 0.005, 0.003 | 1000°C: p=0.018, 0.001, 0.004 | 1200°C: p=0.017, 0.005, 0.014). 30 mol% M consistently gave rise to higher SSA, V_{BJH}, and D_{BJH}. Dopant identity had a statistically significant effect on SSA at 600 (p=0.010) and 1000°C (p=0.019), despite having no statistically measurable effect in the as dried structure. No significance was detected at 1200°C. At 600°C, Y (15%: 125 m^2/g | 30%: 166 m^2/g) and Gd (15%: 127 m^2/g | 30%: 140 m^2/g) were significantly different than Ce (15%: 72 m^2/g | 30%: 85 m^2/g) according to a Tukey test. At 1000°C, Gd (15%: 40 m^2/g | 30%: 50 m^2/g) and Ce (15%: 41 m^2/g | 30%: 49 m^2/g) were significantly different than Yb (15%: 22 m^2/g | 30%: 28 m^2/g).

The evolution of D_{BJH} was found to depend on dopant level, but not identity. Figure 3(c) demonstrates 30 mol% M had a larger average pore size at all temperatures regardless of dopant. Of note is the pore size evolution of the trivalent dopants: Y, Yb, Gd. At 30 mol%, the structures gradually coarsened with increasing temperature, before experiencing a large increase in D_{BJH} from 1000 to 1200°C. At 15 mol%, the structures also coarsened, but only to 1000°C, beyond which D_{BJH} drops precipitously. This behavior was remarkably consistent among the trivalent dopants, which appear to display the same trend, only shifted in absolute value. 15Ca and 15Ce behave similarly to their trivalent counterparts at 15 mol%, but D_{BJH} for 30Ca and 30Ce remains stable from 1000 to 1200°C.

BJH desorption PSDs provided a deeper look at the pore structure as a function of composition and temperature. Figure 4(a-f) includes the PSD of all 10 samples at 600, 1000, and 1200°C, respectively. At 600°C, the PSD for 15 mol% M samples exhibited a high degree of similarity, with sharp distributions set at smaller pore sizes. The trivalent dopants (Y, Yb, Gd) PSDs nearly overlapped at 30 mol%. The area under the PSD is proportional to the total pore volume. By

1000°C, it became evident that 30 mol% M samples are maintaining more porosity than their 15 mol% counterparts for all dopants. This was even more obvious at 1200°C in Figure 4(e), where all 15 mol% distributions are essentially flat, except for 15Gd. Of the 30 mol% samples, 30Y and 30Gd maintained the most porosity made evident by their larger PSD.
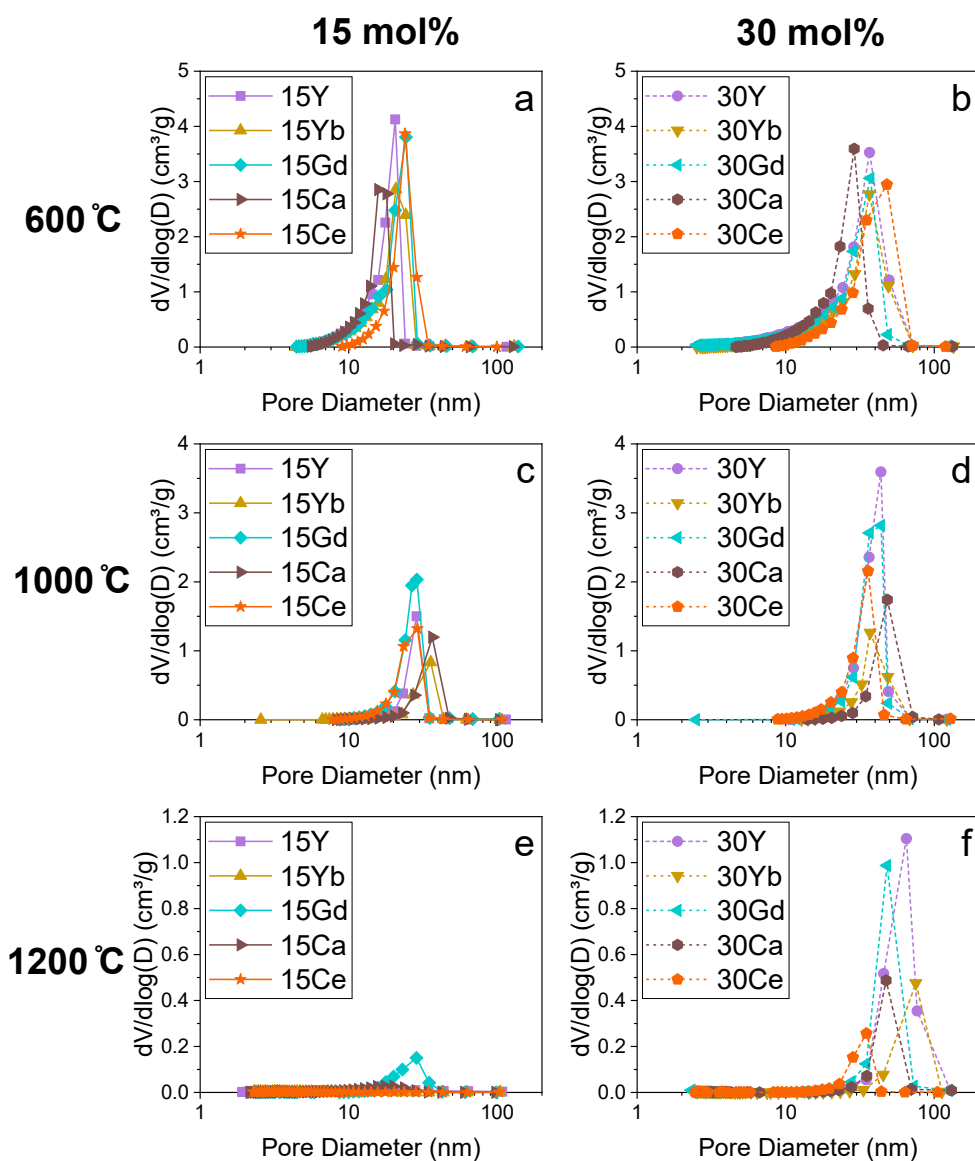

Figure 4(a-f): BJH pore size distributions for 15 mol% (left column) and 30 mol% (right column) as a function of temperature. As the materials are heated, 30 mol% dopant samples in (d) and (f) have increased pore volume compared to their 15 mol% counterparts in (c) and (e). At 1200°C, the only 15 mol% sample to maintain mesoporosity is 15Gd, whereas all 30 mol% samples maintain mesoporosity. Note the scale of the y-axis changes between temperatures.

SEM images were also taken for all samples at each temperature and are included in Figure 5(a-c) at 600, 100, and 1200°C. At 600°C, there was little change from the as dried structure in Figure 2. Only at 1000°C did it become apparent that composition is influencing densification behavior. 15Y, 15Yb, and 15Ca exhibited increased particle growth and coarsening. The other samples maintained their mesoporous structure. At 1200°C, all samples underwent significant particle growth and sintering. In general, 30 mol% M samples maintained smaller particle sizes and some semblance of a porous structure. 15Yb and 15Ce underwent notable sintering by 1200°C, with little mesoporosity visible.

Overall, 30Y and 30Gd displayed the most promising evolution in context of thermal stability. The results thus far evaluate thermal stability in an absolute sense, that is, which samples maintain the highest SSA and V_{BJH} while maintaining a constant D_{BJH}. In the Discussion section, thermal stability will be further evaluated in a relative sense by calculating the percent change or slope of a given property over a selected temperature range. Taking these results together in the context of material properties, a deeper insight may be gained into the thermal stability of highly porous structures at elevated temperatures.

Figure 5(a-c): SEM images after heat treatment at (a) 600°C, (b) 1000°C, and (c) 1200°C. Differences begin to appear at 1000°C for 15Y, 15Yb, and 15Ca with increased particle growth
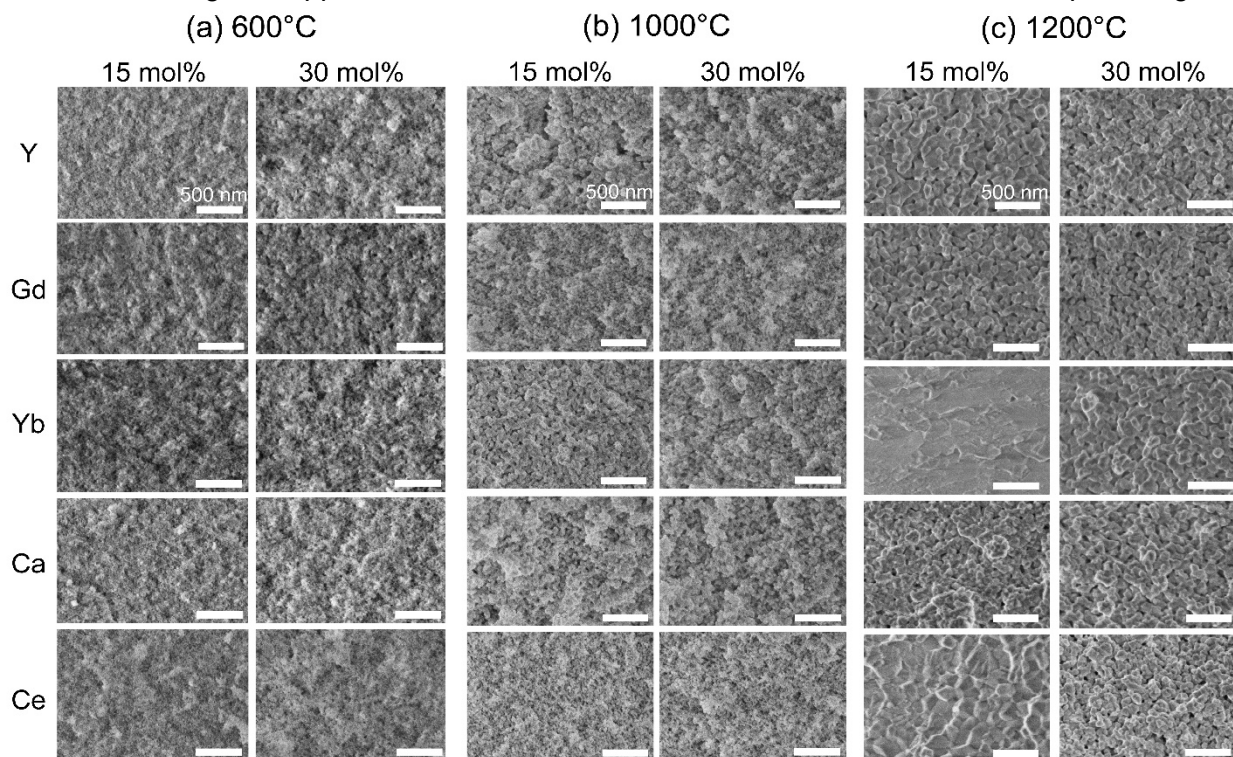
and coarsening. At 1200°C, all samples begin to show coarsening and loss of mesoporosity. The scale bar in all images is 500 nm.

3. Evolution of the crystal structure

In addition to pore structure, the evolution of the crystal structure is an important factor when considering the thermal stability of a highly porous material. Deleterious phase transformations can weaken the structure and rapid crystallite growth may contribute to significant sintering and densification of the fine mesoporous structure. All aerogels were x-ray amorphous as dried. Table 3 includes the phases identified in all materials upon heat treatment. In general, the trivalent dopants crystallized into the cubic (c) structure. 15Ca and 15Ce exhibited a mix of tetragonal (t) and monoclinic (m) phases. 30Ca was consistently cubic and 30Ce tetragonal.

Table 3: Crystalline phases identified in heat treated aerogels (c=cubic, t=tetragonal, m=monoclinic). Y, Yb, and Gd identified as cubic at all temperatures and dopant levels. 30Ca was cubic and 30Ce tetragonal. 15Ca and 15Ce both crystallized into the tetragonal phase, but the monoclinic phase was identified at 1000 and 1200°C.

	mol % MO_x	600°C	1000°C	1200°C
Y	15	c	c	c
	30	c	c	c
Yb	15	c	c	c
	30	c	c	c
Gd	15	c	c	c
	30	c	c	c
Ca	15	t	t, m	t, m
	30	c	c	c
Ce	15	t	t, m	t, m
	30	t	t	t

The XRD patterns were fit in GSASII.[29] The peak widths were used in the Scherrer equation and an average was computed from all peaks to provide a single value of crystallite size (L). The crystallite sizes measured in this work, all under 100 nm, are well within the range of relevance for this technique.[32] The results are summarized in Figure 6 by dopant, dopant level, and temperature. The trivalent dopants shared similar behavior, with higher dopant level suppressing crystallite growth to 1000°C. In general, Gd maintained the smallest crystallites, followed by Y, and finally Yb. From 1000 to 1200°C, the 30 mol% samples underwent significant crystallite growth. The 30Ca aerogel displayed similar behavior and crystallite sizes to the 30 mol% trivalent dopants. The 30Ce aerogel exhibited the most promising behavior as it maintained a single phase and much smaller crystallites than all other samples through 1200°C. At 1200°C, the crystallites for 30Ce were less than half the size of any trivalent dopant. The crystallite growth behavior is markedly more complex in the Ca- and Ce-doped aerogels at 15 mol% M. In these cases, the formation of secondary monoclinic phases modifies the crystallite growth behavior. The tetragonal crystallites in these samples continued to grow, albeit at a reduced rate once the monoclinic phase

was detected. The monoclinic phase, once formed, exhibited a drop in crystallite size from 1000 to 1200°C.

Figure 6: The evolution of crystallite size for all samples, including multiple phases for 15Ca and 15Ce. The trivalent dopants display similar behavior, with higher dopant levels suppressing crystallite growth to 1000°C (Gd < Y < Yb). 30Ce maintained the smallest crystallite size at 1000 and 1200°C for a single-phase sample. The scatter is smaller than the markers, so error bars are
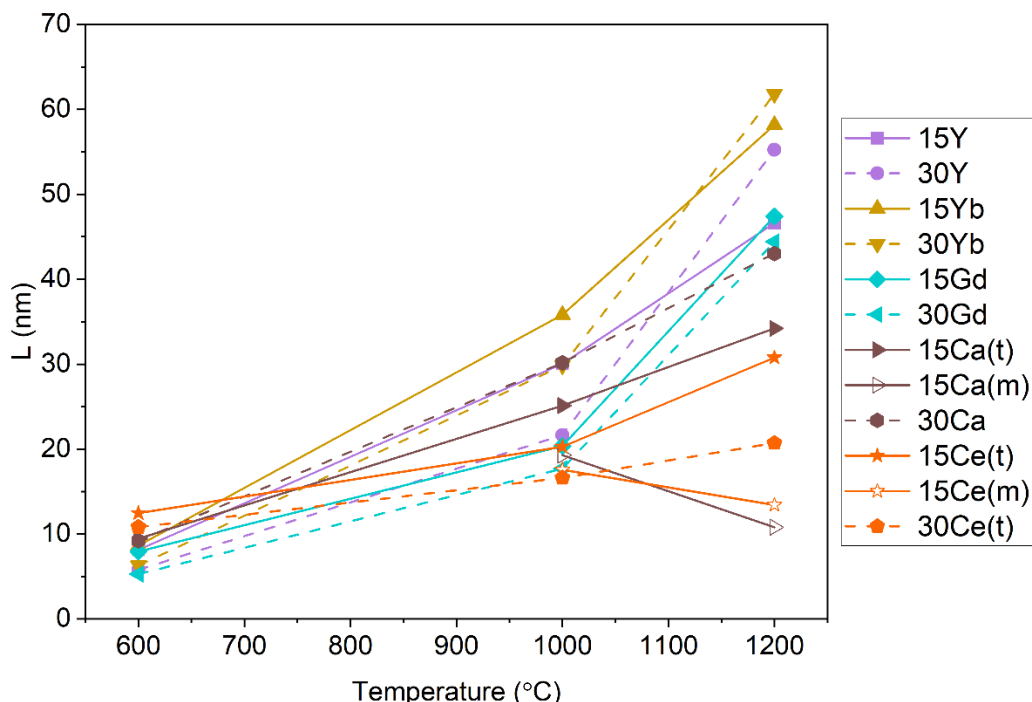
excluded (standard deviation generally lower than 1 nm).

Discussion

1. Effect of dopant level and concentration on the as dried structure

Increased dopant concentration from 15 to 30 mol% MO_x formed coarser pore structures with lower SSA, larger pore volume, larger average pore size, and more disperse pore size distributions. This trend held true for all dopants. This presents a challenge to a hypothesis proposed in our previous work on YSZ aerogels from 0 to 50 mol% $YO_{1.5}$, where a similar trend was observed of coarser pore structures with increasing yttria content.[13] We hypothesized that

with increasing yttria content, the concentration of nucleophile (Cl^-) for epoxide ring opening is higher as $YCl_3 \cdot xH_2O$ provides more chloride than $ZrOCl_2 \cdot xH_2O$. This in turn increases the rate of gelation and results in structures that resemble agglomerated networks of precipitates rather than homogenous gels. The challenge arises for Ca-doped ZrO_2, which should not exhibit this behavior according to our previous hypothesis as $Ca(NO_3)_2 \cdot xH_2O$ does not provide additional nucleophile compared to $ZrOCl_2 \cdot xH_2O$. Despite providing the same amount of nucleophile, 30 mol% CaO formed a coarser pore structure much like the other dopants in the study that do increase nucleophile concentration. To examine this effect and re-evaluate our hypothesis, previous work on epoxide-assisted sol-gel chemistry is informative.[33, 34] Beyond concentration of nucleophiles for the ring opening reaction, the nucleophilicity of chloride compared to the nitrate anion as well as the charge of the metal ions must be considered.

First, it is important to recognize that the calcium precursor is the only nitrate salt used in this study. The hydrated calcium chloride salt is prohibitively expensive if these aerogels are to be used in insulative applications. Previous work by Gash et al. on iron oxide aerogels prepared from chloride and nitrate precursors evaluated the structure of the aerogel as a function of salt anion and solvent.[33] In ethanol, the rate of gel formation was found to be faster for the nitrate salt compared to the chloride salt, despite the nitrate anion being the weaker nucleophile. SSA, pore volume, and pore size were higher for the chloride salt. In the presently studied Ca-doped ZrO_2 aerogels, the pore size was larger at higher mol% CaO, despite the share of nitrate anions increasing, which would be expected to decrease pore size according to the results from Gash. Thus, the difference between chloride and nitrate does not explain the behavior observed in the present work.

The charge of metal ions influences the acidity of hydrated metal cation species, $[M(H_2O)_x]^{x+}$, in solution. As water coordinates to the metal center during hydrolysis, a higher metal coordination number makes the water molecules more acidic. Thus, higher oxidation states will make

19

hydrolysis occur more quickly.[35] A study on mixed metal-silicon oxide aerogels (Al, Cr, Zr, Hf, Nb, Ta, W, and more) by Clapsaddle et al. evaluated the structure of aerogels prepared from hydrated metal salts and propylene oxide.[34] In this work, gel times decreased as coordination number increased, owing to increased acidity and reactivity of the water in the hydrated metal complexes. With shorter gel times, observed shrinkages were higher and the average pore sizes were lower. Longer gel times were generally associated with large particle sizes and coarser pore structures. The authors proposed that with longer gel times, there was more time for nucleation and growth of particles in the sol prior to gelation. Larger particles cannot pack as closely together, leading to reduced shrinkage and larger pore size.

This observation can be applied to the present work to understand the change in structure with increased dopant level. For Y^{3+}, Yb^{3+}, Gd^{3+}, and Ce^{3+}, adding more dopant relative to Zr^{4+} reduces the average oxidation state and acidity of hydrated metal complexes, thereby reducing the reaction rate. Reducing the reaction rate generates coarser structures by allowing more time for nucleation and growth of particles in the sol prior to gelation. The same is true for Ca^{2+}, which again lowers the average oxidation state of metal ions in solution. Although the ratio of nitrate to chloride is increased at higher mol% CaO, it is evident the effect of metal oxidation state is greater than that of changing nucleophile. That said, if the shrinkage and pore size of the Ca-doped aerogels are compared to other dopants, the aerogels did experience more shrinkage and have slightly smaller pore sizes which is consistent with previous work on aerogels derived from nitrate salts, which reduce the gel time and therefore the time for nucleation and growth of particles.

In summary, as the level of dopant is increased from 15 to 30 mol%, a metal with a +4 oxidation state (Zr^{4+}) is being replaced by metals of +2 or +3 oxidation states (Y^{3+}, Yb^{3+}, Gd^{3+}, Ce^{3+}, Ca^{2+}) This reduces the reaction rate by reducing the acidity of water in the hydrated metal complexes, allowing for more nucleation and growth in the sol prior to gelation. This results in coarser

structures composed of larger particles that exhibit lower shrinkages and broader pore size distributions.

2. Evaluation of thermal stability

It is prudent to first define by what metrics thermal stability may be evaluated in the context of aerogels. The most relevant assessment of thermal stability is maintaining a highly porous structure conducive to low thermal conductivity. The loss of porosity should be minimized by maximizing SSA and pore volume. By minimizing change in pore size, thermal conductivity and other transport properties can be maintained at a similar value through the operating temperature range of the material. Limiting phase transformations and crystallite growth will ensure structural integrity of the aerogel. All of the metrics can be evaluated in an absolute sense, that is directly comparing the SSA or any other property of one formulation to another at a given temperature. This is the simplest method by which thermal stability can be evaluated.

As covered in the Results, increased dopant concentration lends improved thermal stability, with select dopants outperforming the rest. At 1000°C, 30 mol% Ce, Gd, and Y maintain the highest SSA and pore volume. At 1200°C, 30 mol% Gd and Y perform the best. It is important to note increased dopant concentration also changed the as dried structure, forming coarser structures with larger initial pore sizes. The coarser structure with higher dopant concentration should reduce the driving force for sintering and densification, improving thermal stability. The effect of starting structure on thermal stability was evaluated in another work.[36] The analysis therein suggests the differences in as dried structure between 15 and 30 mol% dopant should not have a significant effect on thermal stability. Therefore, the effect is believed to be the result of the increased dopant concentration and not the change in the as dried structure.

It is also possible to evaluate relative stability, which looks at how a property changes over a selected temperature range. This method of evaluation can give insight to what degree a

material's structure changes over a given operating range of temperatures. Information on the evolution of the materials may be gleaned by calculating the percent change (Equation 1) or slope (Equation 2) of a property over a temperature interval. X represents a structural property, such as SSA, V_{BJH}, or D_{BJH} and T is temperature in degrees Celsius. In this work, all materials are highly porous as dried, and it is ultimately the ability to minimize the change in structure that will prove advantageous when applied as insulation. For SSA, pore size, and pore volume, calculation of percent change will be applied to evaluate relative stability, with lower percent change reflecting higher thermal stability. For crystallite size, calculation of slope will be applied to evaluate relative stability. Since the crystallite size is effectively zero in the initial as dried, x-ray amorphous state, the initial value of crystallite size upon crystallization can undesirably affect the comparison of thermal stability when percent change is applied. It allows for the comparison of the responses of materials that have different starting structures.

$$Percent\ Change\ = \frac{X_{Final} - X_{Initial}}{X_{Initial}} \times 100\% \qquad \textbf{Equation 1}$$

$$Slope\ = \frac{X_{Final} - X_{Initial}}{T_{Final} - T_{Initial}} \qquad \textbf{Equation 2}$$

Relative stability may be evaluated over the entire temperature range or select temperature ranges. Comparison of materials over different temperature ranges is useful for potential applications and their unique operating temperature ranges. Figure 7 displays the percent change of SSA, pore volume, and pore size over three temperature ranges: as dried to 600°C, 600 to 1000°C, and 1000 to 1200°C. Figure 8 shows the slope of crystallite size from 600 to 1000°C and 1000 to 1200°C.
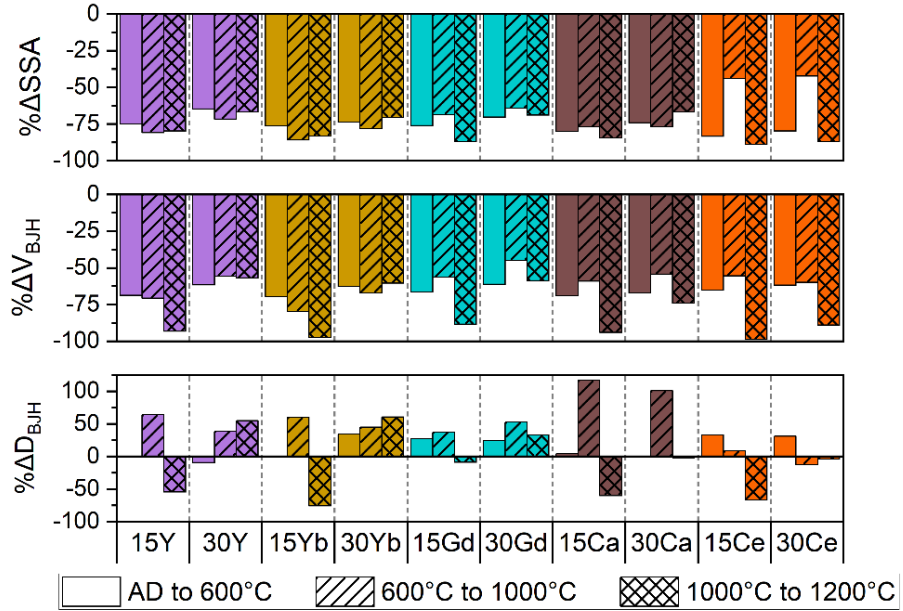
Figure 7: The percent change of SSA, V_{BJH}, and D_{BJH} from AD to 600°C, 600 to 1000°C, and 1000 to 1200°C. The change in SSA and V_{BJH} permit stability over a given temperature range to be evaluated. As an example, doping with Ce leads to rapid loss of porosity from AD to 600°C and 1000 to 1200°C, but improved stability from 600 to 1000°C.
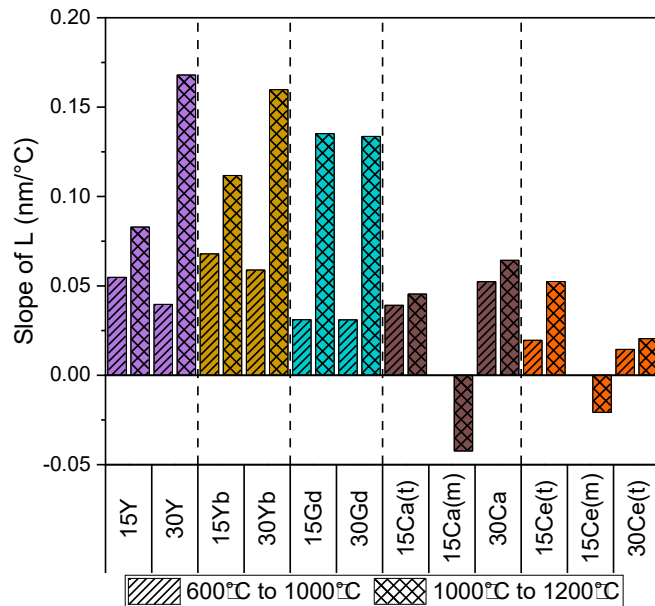
Figure 8: The slope of crystallite size from 600 to 1000°C and 1000 to 1200°C for each material and unique phase. All materials were cubic phase unless otherwise noted (t=tetragonal, m=monoclinic). For Y, Yb, and Gd, increased dopant concentration generally suppresses crystallite growth from 600 to 1000°C, but 30 mol% samples grow rapidly from 1000 to 1200°C. The crystallite growth of 15Ca and 15Ce is complicated by the phase changes experienced in those samples. 30Ce maintains a single phase and undergoes minimal crystallite growth relative to other samples.

23

For analysis within this study, the change from the as dried structure to 1000°C was selected for SSA, pore size, and pore volume and change from 600 to 1200°C for crystallite size. The values of percent change and slope are included in Table 4. Dopant identity ($p=0.016$) and concentration ($p=0.010$) had significant effects on the percent change of SSA from as dried to 1000°C, with 30 mol% dopant retaining more SSA. From a Tukey test, there were three different groups of dopants for retention of SSA, listed here in descending order of stability: Ce/Gd/Y, Gd/Y/Ca, Y/Ca/Yb. Though 30 mol% Ce performed the best in terms of relative stability to 1000°C, this composition rapidly densified from 1000 to 1200°C. This demonstrates the importance of considering both relative and absolute stability, as well as considering different temperatures and ranges depending on the application.

Dopant identity had a significant effect ($p=0.013$) on crystallite growth, but the concentration did not ($p=0.384$). There were two significantly different groups of dopants: Y/Yb/Gd/Ca and Ca/Ce. Yb, Y, and Gd experienced the most crystallite growth, but were also the most phase stable. Within the series of trivalent dopants, smaller ionic radius was associated with increased crystallite growth. Despite minimizing crystallite growth, phase stability may be a disadvantage with Ce and Ca. The exception is 30 mol% Ce, which maintained a single tetragonal phase and the least crystallite growth. This composition also maintained a stable pore structure to 1000°C, but densified rapidly upon exposure to 1200°C.

Table 4: The percent change of SSA, V_{BJH}, and D_{BJH} from the as dried state to 1000°C. The slope of crystallite size (L) is calculated from 600 to 1200°C. Samples with best overall thermal stability to 1000°C are 30Y, 30Gd, and 30Ce. For all samples, increased dopant concentration reduced the amount of densification experienced.

M	mol % MO_x	SSA (%)	V_{BJH} (%)	D_{BJH} (%)	L (nm•°C^{-1})
Y	15	-95.2	-90.9	63.6	0.064
	30	-90.1	-83.1	26.2	0.082
Yb	15	-96.7	-93.9	60.1	0.083
	30	-94.3	-87.7	94.4	0.093
Gd	15	-92.5	-85.5	75.3	0.066
	30	-89.3	-78.7	90.1	0.065
Ca	15	-95.4	-87.4	125.1	0.041
	30	-94.0	-85.0	98.6	0.056
Ce	15	-90.7	-84.4	43.8	0.031
	30	-88.4	-84.7	14.7	0.014

*3. Towards a design framework for thermally stable aerogels*

In the present work, many dopants were evaluated, but material properties are not readily available for the entire range of materials studied. Cation properties, such as radius, mass, and charge, may serve as useful proxies for other material properties. The properties can be weighted by cation composition to reveal the effect of changing radius, mass, and charge. This is demonstrated in Equation 3, where x_M is the mole fraction MO_y and P_M is the property of dopant M^{2y+}. The weighted properties were then scaled on [0, 1] to allow for comparison between radius, mass, and charge on the same plot.

$$Weighted\ Property\ =\ x_{Zr}P_{Zr} + x_M P_M \qquad \textbf{Equation 3}$$

The thermal stability as a function of the weighted property can be evaluated in an absolute or relative sense. For absolute stability, the SSA, pore volume, pore size, and crystallite size were taken at 1000°C and plotted as a function of the scaled and weighted cation properties in Figure 9(a-d), respectively. Linear regression was then performed. Cation radius and charge did

influence the pore structure at 1000°C. Increased radius was associated with higher pore volume (p=0.04) and larger pore size (p<0.001). Increased charge was associated with smaller pore size (p<0.001). Linear regression was similarly performed for relative stability (percent change, slope) as shown in Figure 10(a-d), but no statistically significant relationships were identified.

Additional work is required to bring together property and performance measurement to improve the design of thermally stable aerogels. Despite the fact that radius, charge, and mass of the cation do not have clear effects on thermal stability, many material properties have complex relationships with these cation descriptors. Well-designed experiments, especially coupled with simulation, measuring material properties and thermal stability will enable further design rule development.
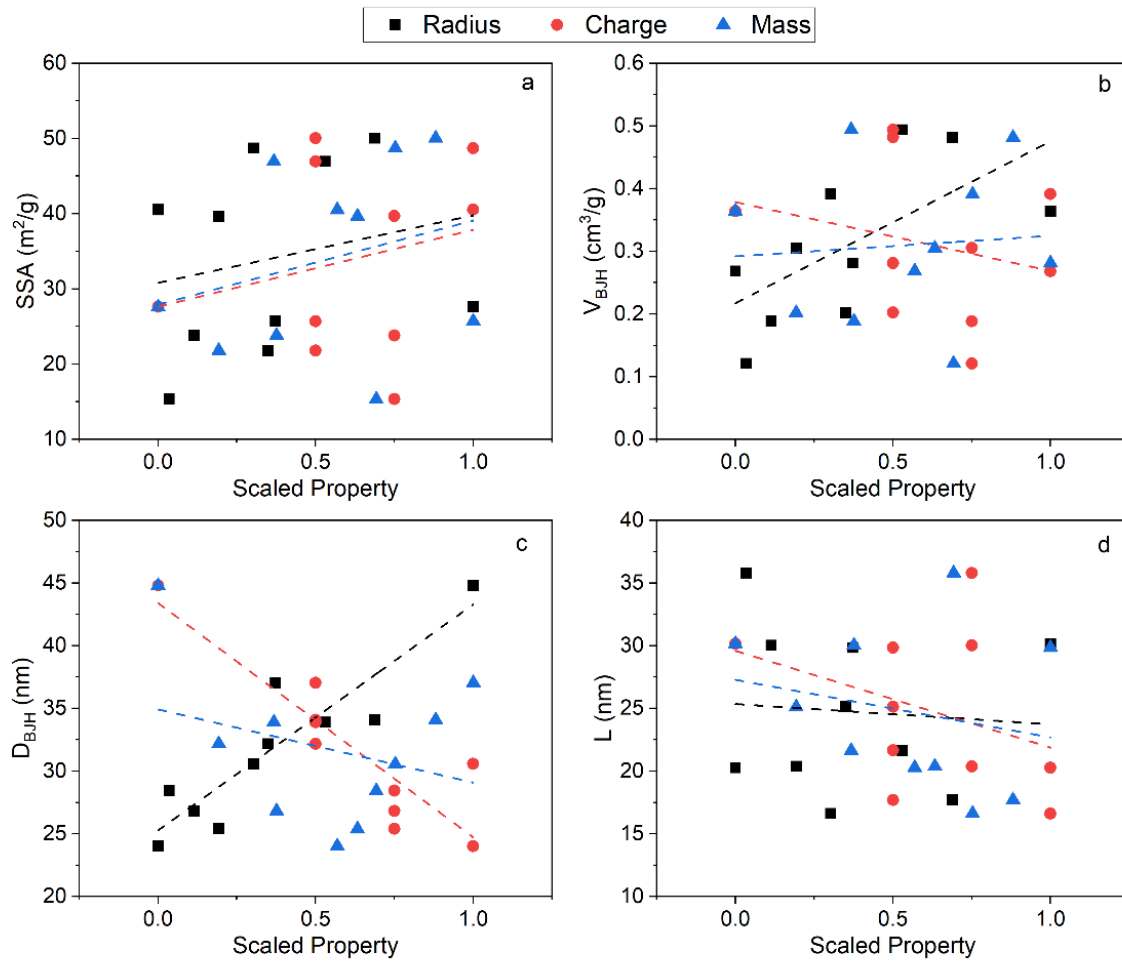
Figure 9(a-d): The (a) SSA, (b) V_{BJH}, (c) D_{BJH}, and (d) crystallite size, all after 1000°C heat treatment, as a function of weighted properties of cation radius, charge, and mass. Statistical analysis was then performed to identify significant effects of weighted properties on aerogel structure. Increased radius was associated with higher pore volume (p=0.04) and larger pore size (p<0.001). Increased charge was associated with smaller pore size (p<0.001).
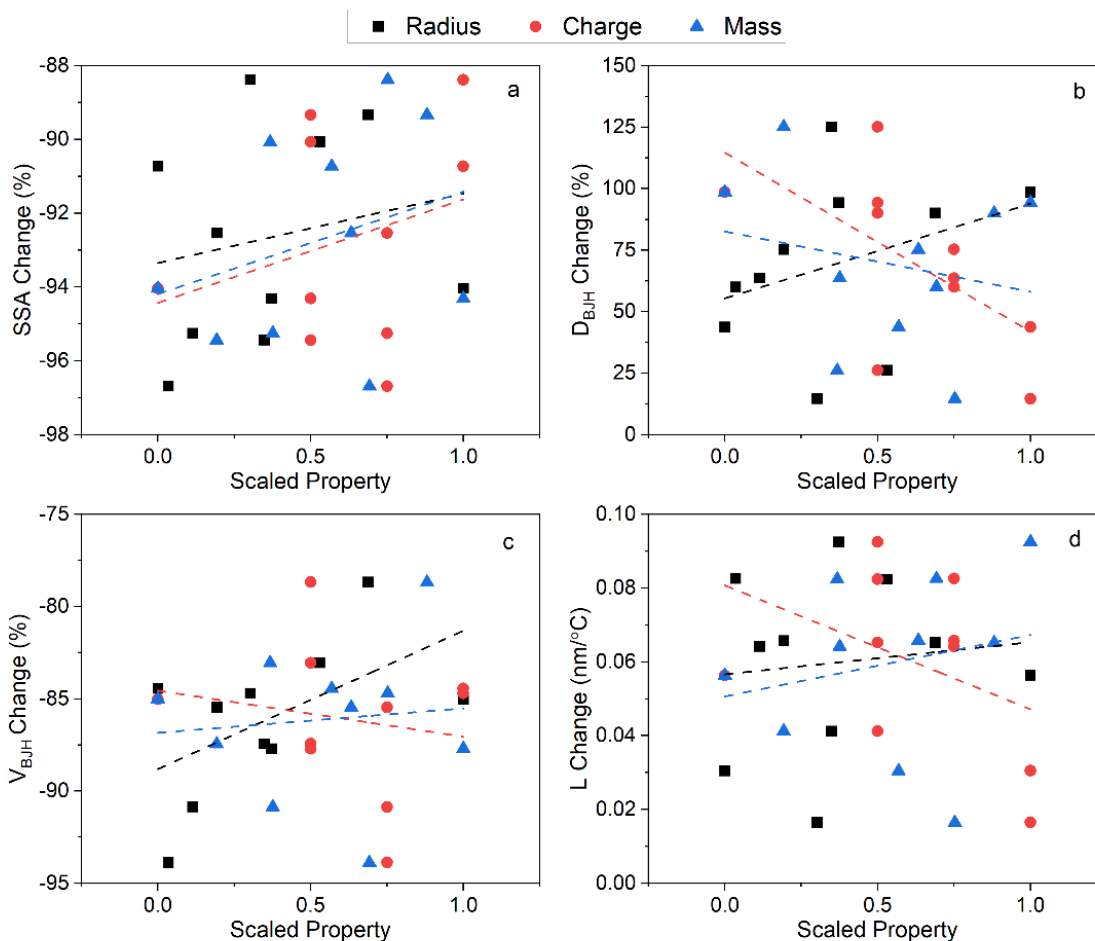
Figure 10(a-d): The percent change of (a) SSA, (b) V_{BJH}, (c) D_{BJH}, and (d) crystallite size from AD to 1000°C as a function of weighted properties of cation radius, charge, and mass. No statistically significant relationships were identified in this analysis.

Lastly, the magnitude of changes to thermal stability as a function of composition must be considered. Though statistically significant differences were observed in this work, none are arguably large enough to consider any of the presently studied pore structures "thermally stable". Here, we probed the extremes of doped zirconia. Previous work studying composition's influence on thermal stability has led to mixed results. Aerogels composed of TiO_2, Nb_2O_5, and ZrO_2 aerogels maintained SSAs that varied by a factor of 3 at 500°C, but this same variation was observed in the as dried state.[11] Oxide aerogels of Ce, Pr, Sm, and Tb were prepared with SSAs of 250, 296, 129, and 147 m^2/g, respectively, and maintained SSAs of 60, 60, 90, and 90 m^2/g

after heat treatment at 650°C.[10] Looking at this wide range of metal oxides with varying properties and as dried SSAs, the difference in thermal stability was small. Doping alumina with yttria and zirconia with yttria and/or ytterbia improved thermal stability.[8, 12, 13] These doped aerogels offered improved thermal stability to 1000°C, but any advantage was consistently eliminated beyond this temperature.

More impactful routes to thermal stability may include new synthetic techniques and post-synthetic modification of aerogels to improve the robustness of the structure towards densification. Comparing soluble precursors (metal salts) to colloidal boehmite in the preparation of aluminosilicate aerogels demonstrated the dramatic influence of synthetic route on the structure, chemistry, and thermal stability of aerogels.[9] The effect of precursor and synthetic route goes beyond simply changing the SSA and pore size for a given composition, rather emerging from the morphology of the precursor, connectivity of primary particles, and the spatial distribution of constituents in multi-oxide aerogels. The improved stability of the boehmite derived materials might be attributable to the boehmite being crystalline to start, eliminating the shrinkages associated with the crystallization of an amorphous as-dried gel. Continued work on novel colloidal syntheses of aerogels may serve as useful routes towards the development of thermally stable aerogels.[37, 38] Modification of aerogel structures with post-synthetic coatings and functional groups has proven effective to have marked improvement on thermal stability.[39, 40] Such approaches prevent condensation of surface hydroxyl groups by capping hydroxyl groups with non-condensable functional groups which then form secondary-phase particles that pin grain boundaries and prevent crystallite growth at higher temperatures. Overall, advances in aerogel synthesis may prove the most effective means of achieving thermal stability and enabling the use of aerogel as insulation in extreme environments. The advances must go beyond straightforward synthetic parameters and leverage novel precursors, assembly techniques, and post-synthetic modifications to enhance thermal stability.

Conclusions

Doped zirconia aerogels of 15 and 30 mol% M/(M+Zr) where M = Y, Yb, Gd, Ce, Ca were synthesized from metal salt precursors and supercritically dried. Higher dopant concentration formed coarser pore structures with broader pore size distributions and larger average pore sizes. This result was linked to the reduction in average metal oxidation state in solution with increased dopant level. The thermal stability as a function of composition was evaluated in absolute terms, with 30 mol% $GdO_{1.5}$ and $YO_{1.5}$ maintaining the highest SSA and pore volume to 1200°C. In general, increased dopant concentration improved the thermal stability for all dopants at 1200°C. Relative stability was also used to compare thermal stabilities, again with increased dopant concentration lending improved thermal stability and Y and Gd performing the best of all dopants. Attempts to derive relationships between thermal stability and weighted cation properties (charge, mass, size) were largely unsuccessful, with only a few statistically significant relationships. Overall, the magnitude of thermal stability improvement achieved by modifying dopant identity and concentration was considered in context to other routes, including modification of synthetic techniques. This comparison points towards the fact that development of new synthetic techniques will likely offer the greatest chance at achieving the thermal stability required to use aerogels as insulation in the extreme environments of aerospace applications.

Acknowledgements

References

1. Pierre AC, Pajonk GM. Chemistry of aerogels and their applications. *Chemical Reviews*. 2002;102(11):4243–4265. https://doi.org/10.1021/cr0101306

2. Lee JK, Gould G. Polyolefin-Based Aerogels. *NASA Tech*. 2012;(November 2012):14.

3. Kim J, Kwon J, Kim SI, *et al.* One-step synthesis of nano-porous monolithic polyimide aerogel. *Microporous and Mesoporous Materials*. 2016;234:35–42. https://doi.org/10.1016/j.micromeso.2016.06.037

4. Hu P, Liu L, Zhao M, Wang J, Ma X, Wang J. Design, Synthesis, and Use of High Temperature Resistant Aerogels Exceeding 800 oC. *ES Materials & Manufacturing*. 2021;14–33. https://doi.org/10.30919/esmm5f459

5. Hench LL, West JK. The sol-gel process. *Chemical Reviews*. 1990;90(1):33–72. https://doi.org/10.1021/cr00099a003

6. Emmerling A, Gross J, Gerlach R, *et al.* Isothermal sintering of SiO2-aerogels. *Journal of Non-Crystalline Solids*. 1990;125(3):230–243. https://doi.org/10.1016/0022-3093(90)90853-E

7. Folgar C, Folz D, Suchicital C, Clark D. Microstructural evolution in silica aerogel. *Journal of Non-Crystalline Solids*. 2007;353:1483–1490. https://doi.org/10.1016/j.jnoncrysol.2007.02.047

8. Al-Yassir N, Le Van Mao R. Thermal stability of alumina aerogel doped with yttrium oxide, used as a catalyst support for the thermocatalytic cracking (TCC) process: An investigation of its textural and structural properties. *Applied Catalysis A: General*. 2007;317(2):275–283. https://doi.org/10.1016/j.apcata.2006.10.030

9. Hurwitz FI, Gallagher M, Olin TC, *et al.* Optimization of Alumina and Aluminosilicate Aerogel Structure for High-Temperature Performance. *International Journal of Applied Glass Science*. 2014;5(3):276–286. https://doi.org/10.1111/ijag.12070

10. Clapsaddle BJ, Neumann B, Wittstock A, *et al.* A sol-gel methodology for the preparation of lanthanide-oxide aerogels: Preparation and characterization. *Journal of Sol-Gel Science and Technology*. 2012;64(2):381–389. https://doi.org/10.1007/s10971-012-2868-6

11. Suh DJ, Park TJ. Sol-gel strategies for pore size control of high-surface-area transition-metal oxide aerogels. *Chemistry of Materials*. 1996;8(2):509–513. https://doi.org/10.1021/cm950407g

12. Hurwitz FI, Rogers RB, Guo H, *et al.* Phase development and pore stability of yttria- and ytterbia-stabilized zirconia aerogels. *Journal of the American Ceramic Society*. 2020;103(12):6700–6711. https://doi.org/10.1111/jace.17376

13. Olson NS, Hurwitz FI, Guo H, *et al.* Enhanced thermal stability of high yttria concentration YSZ aerogels. *Journal of the American Ceramic Society*. 2021;(February):1–13. https://doi.org/10.1111/jace.17792

14. Zhu D, Miller RA. Thermal Conductivity and Sintering Behavior of Advanced Thermal Barrier Coatings. *26th Annual Conference on Composites, Advanced Ceramics, Materials, and Structures*. 2002 https://doi.org/10.1002/9780470294758.ch51

15. Winter MR, Clarke DR. Oxide materials with low thermal conductivity. *Journal of the American Ceramic Society*. 2007;90(2):533–540. https://doi.org/10.1111/j.1551-2916.2006.01410.x

16. Clarke DR. Materials Selection Guidelines for Low Thermal Conductivity Thermal Barrier Coatings Temperature Dependence of Thermal Conductivity Models for Thermal Conductivity. *Surface and Coatings Technology*. 2003;163–164:67–74. https://doi.org/dx.doi.org/doi:10.1016/S0257-8972(02)00593-5

17. Clarke DR, Levi CG. Materials Design for the Next Generation Thermal Barrier Coatings. *Annual Review of Materials Research*. 2003;33(1):383–417. https://doi.org/10.1146/annurev.matsci.33.011403.113718

18. Clarke DR, Phillpot SR. Thermal barrier coating materials. *Materials Today*. 2005;8(6):22–29. https://doi.org/10.1016/S1369-7021(05)70934-2

19. Levi CG. Emerging materials and processes for thermal barrier systems. *Current Opinion in Solid State and Materials Science*. 2004;8(1):77–91. https://doi.org/10.1016/j.cossms.2004.03.009

20. Boulc'h F, Dessemond L, Djurado E. Dopant size effect on structural and transport properties of nanometric and single-phased TZP. *Solid State Ionics*. 2002;154–155:143–150. https://doi.org/10.1016/S0167-2738(02)00422-8

21. Yi H, Che J, Liang G, Liu Z. Effect of Rare Earth Elements on Stability and Sintering Resistance of Tetragonal Zirconia for Advanced Thermal Barrier Coatings. *Crystals*. 2021;11(287).

22. Quach D V., Castro RHR. Direct measurement of grain boundary enthalpy of cubic yttria-stabilized zirconia by differential scanning calorimetry. *Journal of Applied Physics*. 2012;112(8):3–8. https://doi.org/10.1063/1.4761992

23. Nafsin N, Li H, Leib EW, Vossmeyer T, Stroeve P, Castro RHR. Stability of rare-earth-doped spherical yttria-stabilized zirconia synthesized by ultrasonic spray pyrolysis. *Journal of the American Ceramic Society*. 2017;100(10):4425–4434. https://doi.org/10.1111/jace.14971

24. Li H, Dey S, Castro RHR. Kinetics and thermodynamics of densification and grain growth: Insights from lanthanum doped zirconia. *Acta Materialia*. 2018;150:394–402. https://doi.org/10.1016/j.actamat.2018.03.033

25. Castro RHR, Gouvêa D. Sintering and Nanostability: The Thermodynamic Perspective. *Journal of the American Ceramic Society*. 2016;99(4):1105–1121. https://doi.org/10.1111/jace.14176

26. Drazin JW, Castro RHR. Phase stability in nanocrystals: A predictive diagram for yttria-zirconia. *Journal of the American Ceramic Society*. 2015;98(4):1377–1384. https://doi.org/10.1111/jace.13504

27. Kilo M, Borchardt G, Lesage B, Katasov O, Weber S, Scherrer S. Cation transport in yttria stabilized cubic zirconia: 96Zr tracer diffusion in (ZrxY1-x)O2-x/2 single crystals with 0.15≤x≤0.48. *Journal of the European Ceramic Society*. 2000;20(12):2069–2077. https://doi.org/10.1016/S0955-2219(00)00072-8

28. Gash AE, Tillotson TM, Satcher JH, Hrubesh LW, Simpson RL. New sol-gel synthetic route to transition and main-group metal oxide aerogels using inorganic salt precursors. *Journal of Non-Crystalline Solids*. 2001;285(1–3):22–28. https://doi.org/10.1016/S0022-3093(01)00427-6

29. Toby BH, Von Dreele RB. GSAS-II: The genesis of a modern open-source all purpose crystallography software package. *Journal of Applied Crystallography*. 2013;46(2):544–549. https://doi.org/10.1107/S0021889813003531

30. Shannon RD. Revised effective ionic radii and systematic studies of interatomic distances in halides and chalcogenides. *Acta Cryst A*. 1976;32(5):751–767. https://doi.org/10.1107/S0567739476001551

31. Shannon RD, Prewitt CT. Effective ionic radii in oxides and fluorides. *Acta Crystallogr B Struct Sci*. 1969;25(5):925–946. https://doi.org/10.1107/S0567740869003220

32. Holzwarth U, Gibson N. The Scherrer equation versus the "Debye-Scherrer equation." *Nature Nanotech*. 2011;6(9):534–534. https://doi.org/10.1038/nnano.2011.145

33. Gash AE, Tillotson TM, Satcher JH, Poco JF, Hrubesh LW, Simpson RL. Use of Epoxides in the Sol-Gel Synthesis of Porous Iron(III) Oxide Monoliths from Fe(III) Salts. *Chemistry of Materials*. 2001;13(3):999–1007. https://doi.org/10.1021/cm0007611

34. Clapsaddle BJ, Sprehn DW, Gash AE, *et al.* A versatile sol-gel synthesis route to metal-silicon mixed oxide nanocomposites that contain metal oxides as the major phase. *Journal*

of Non-Crystalline Solids. 2004;350:173–181.

https://doi.org/10.1016/j.jnoncrysol.2004.06.025

35. Baes CF, Mesmer RE. The Hydrolysis of Cations. Wiley; 1976

36. Meyer J, Olson NS, Hurwitz FI, Guo H, Stokes JL, Krogstad JA. Effect of synthetic

    parameters on structure and thermal stability in yttria-stabilized zirconia aerogels. *Journal*

    of the American Ceramic Society. n.d.;In preparation.

37. Matter F, Luna AL, Niederberger M. From colloidal dispersions to aerogels: How to master

    nanoparticle gelation. *Nano Today*. 2020;30:100827.

    https://doi.org/10.1016/j.nantod.2019.100827

38. Rechberger F, Niederberger M. Synthesis of aerogels: From molecular routes to 3-

    dimensional nanoparticle assembly. *Nanoscale Horizons*. 2017;2(1):6–30.

    https://doi.org/10.1039/c6nh00077k

39. Wu NL, Wang SY, Rusakova IA. Inhibition of crystallite growth in the sol-gel synthesis of

    nanocrystalline metal oxides. *Science*. 1999;285(5432):1375–1377.

    https://doi.org/10.1126/science.285.5432.1375

40. Zu G, Shen J, Wang W, *et al.* Robust, highly thermally stable, core-shell nanostructured

    metal oxide aerogels as high-temperature thermal superinsulators, adsorbents, and

    catalysts. *Chemistry of Materials*. 2014;26(19):5761–5772.

    https://doi.org/10.1021/cm502886t

Author Contributions

Nathaniel S. Olson – Lead on experimentation, analysis, and writing original draft. Conducted editing and final review

Frances I. Hurwitz – Advisor on experimental design and analysis. Contributed to writing, reviewing, and editing drafts

Jamesa L. Stokes – Advisor on experimental design and analysis. Contributor to data analysis, specifically x-ray diffraction. Contributed to writing, reviewing, and editing drafts

Haiquan Guo – Contributor to experimentation. Advisor on experimental design and analysis. Contributed to reviewing and editing drafts.

Richard B. Rogers – Contributor and advisor on experimentation and analysis, specifically x-ray diffraction data collection and analysis. Contributed to reviewing and editing drafts.

Jessica A. Krogstad – Advisor on experimental design and analysis. Contributed to writing, reviewing, and editing all drafts.